communications earth & environment

Article

https://doi.org/10.1038/s43247-024-01324-8

Recent reductions in aerosol emissions have increased Earth's energy imbalance

Øivind Hodnebrog[1] ✉, Gunnar Myhre[1], Caroline Jouan[1], Timothy Andrews[2], Piers M. Forster[3], Hailing Jia[4,9], Norman G. Loeb[5], Dirk J. L. Olivié[6], David Paynter[7], Johannes Quaas[4], Shiv Priyam Raghuraman[8] & Michael Schulz[6]

The Earth's energy imbalance is the net radiative flux at the top-of-atmosphere. Climate model simulations suggest that the observed positive imbalance trend in the previous two decades is inconsistent with internal variability alone and caused by anthropogenic forcing and the resulting climate system response. Here, we investigate anthropogenic contributions to the imbalance trend using climate models forced with observed sea-surface temperatures. We find that the effective radiative forcing due to anthropogenic aerosol emission reductions has led to a 0.2 ± 0.1 W m^{-2} decade^{-1} strengthening of the 2001–2019 imbalance trend. The multi-model ensemble reproduces the observed imbalance trend of 0.47 ± 0.17 W m^{-2} decade^{-1} but with 10-40% underestimation. With most future scenarios showing further rapid reductions of aerosol emissions due to air quality legislation, such emission reductions may continue to strengthen Earth's energy imbalance, on top of the greenhouse gas contribution. Consequently, we may expect an accelerated surface temperature warming in this decade.

The Earth's Energy Imbalance (EEI) is the difference in the net downward shortwave (SW) radiative flux and outgoing longwave (LW) radiative flux at the top-of-atmosphere (TOA). It causes changes in the heat content of the oceans, ice, land, and atmosphere, and is principally estimated by looking at in situ observations of the heat content of the oceans, which absorb approximately 90% of the excess heat due to EEI[1]. Recent estimates for the 2010–2022 period give a value of 0.89 ± 0.26 W m^{-2} (ref. [2]), increasing from the value of 0.79 ± 0.27 W m^{-2} for 2006–2018 reported in the Intergovernmental Panel on Climate Change (IPCC) Assessment Report 6 (AR6)[3]. The mean EEI from the Clouds and the Earth's Radiant Energy System (CERES) is constrained by adjusting SW and LW TOA fluxes within their ranges of uncertainty such that the mean EEI from CERES for 07/2005-06/2015 is consistent with EEI from in situ observations for the same period[4,5]. Variations in EEI from CERES are independent of in situ data and have been demonstrated to be especially useful for examining trends in EEI[6]. Two decades of satellite observations are now available from CERES, and show a positive 2005–2019 trend in the EEI of 0.50 ± 0.47 W m^{-2} decade^{-1} (ref. [6]). The CERES trend is in agreement with ocean-derived trends[1,2]. Single climate model simulations indicate that the recent trend is only explained when anthropogenic forcing and response are included[7].

The EEI can be seen as the sum of effective radiative forcing (ERF), which includes rapid adjustments to natural and anthropogenic instantaneous radiative forcing, and the radiative response to the forcing, which is the result of global mean surface temperature change (ΔT_s) and associated climate feedbacks (α)[3,7]. Thus, a positive EEI confirms the lag of the climate system in responding to forcing and implies that additional global warming will take place even without further forcing changes[8]. On shorter time scales, EEI is modulated by internal variability such as the El-Niño Southern Oscillation (ENSO)[9].

The recent positive trend in EEI is mainly caused by reductions in the reflection of SW radiation while LW radiation changes are smaller and slightly reduce the positive net EEI trend[7]. The latest generation global climate models (GCMs) are able to reproduce the pattern of TOA radiative flux changes from CERES relatively well when forced with observed sea-surface temperature (SST) and sea-ice until 2017[10], but model simulations for a longer time period (until 2019/2020) indicate an underestimation of

[1]Center for International Climate Research (CICERO), Oslo, Norway. [2]Met Office Hadley Centre, Exeter, UK. [3]Priestley Centre for Climate Futures, University of Leeds, Leeds, UK. [4]Institute for Meteorology, Leipzig University, Leipzig, Germany. [5]NASA Langley Research Center, Hampton, VA, USA. [6]Norwegian Meteorological Institute, Oslo, Norway. [7]NOAA Geophysical Fluid Dynamics Laboratory, Princeton, NJ, USA. [8]Rosenstiel School of Marine, Atmospheric, and Earth Science, University of Miami, Coral Gables, FL, USA. [9]Present address: SRON Netherlands Institute for Space Research, Leiden, The Netherlands.
✉e-mail: oivind.hodnebrog@cicero.oslo.no

the EEI trend, especially in the SW[7,11]. At the same time, previous model studies have often not accounted for recent changes in anthropogenic forcings (e.g., aerosol emissions) and/or radiative response (i.e., SST and sea-ice fields), and assumptions made regarding these input data could have a large influence on the modelled trends. Over China, the decline of SO_2 emissions after 2007 is not represented in the emission inventory used in Coupled Model Intercomparison Project phase 6 (CMIP6)[12]. The trend in instantaneous and effective radiative forcing due to cooling aerosols has reversed, now showing a robust positive trend for both aerosol-radiation interactions (ERFari) and aerosol-cloud interactions (ERFaci)[13,14], suggesting a temporary acceleration in the rate of warming[15]. The influence of aerosols on cloud fraction and other cloud properties is uncertain, however, and recent models show difficulties in reproducing satellite observations[16,17].

While our study addresses some of the same research questions as Raghuraman, et al.[7], we do so using a multi-model multi-ensemble approach, recognising the substantial diversity in aerosol ERF among models. Further, our study incorporates innovative simulations to isolate the contributions of anthropogenic aerosol forcing to the trend in EEI. We have performed simulations forced with observed SST and sea-ice from 2000–2019 and where the aerosol emissions are based on an inventory that better accounts for the recent emission reductions compared to the inventory used in the CMIP6 simulations (see Methods). Simulations are compared to CERES and Moderate Resolution Imaging Spectroradiometer (MODIS) satellite observations of radiative fluxes[18], Aerosol Optical Depth (AOD)[19] and cloud properties[20]. Additionally, dedicated sensitivity experiments are conducted to further elucidate the factors contributing to the observed positive trend in EEI.

We find that observed trends in aerosol optical depth are very well reproduced by the model mean over regions of anthropogenic emissions and that the ERF due to recent anthropogenic aerosol emission reductions has contributed substantially to the increase in Earth's energy imbalance observed during the period 2001–2019. The trend in shortwave flux drives the EEI trend and is caused by approximately equal contributions from aerosol ERF and radiative response to the total forcing.

Results and discussion

Global EEI trend

Observations from the CERES satellite product reveal a significant and positive trend in the Earth's energy imbalance since the beginning of the 2000s, with a January 2001–December 2019 (January 2001–June 2023) trend of 0.47 ± 0.17 (0.51 ± 0.17) W m^{-2} decade^{-1} based on deseasonalized monthly data (Fig. 1a; Supplementary Fig. 1). The interannual variability is considerable and, with a few exceptions, very well reproduced by the GCMs; all five models show a correlation coefficient (between models and CERES) greater than 0.7 (Fig. 1a). The models reproduce a positive trend but the ensemble mean trend for each model is weaker than in CERES, with approximately 10 to 40% underestimation. The positive EEI trend in CERES and models is also in agreement with estimates of ocean heat content anomalies for 2005-2019 (Supplementary Fig. 2).

The weakest EEI trend is seen in the GFDL simulations (Fig. 1a), which have used CMIP6 aerosol emissions, in contrast to most of the other models (see Methods). However, sensitivity simulations with CESM2 indicate that the difference in the EEI trend between simulations using aerosol emissions as in CMIP6 (assuming SSP2-4.5 from 2015 onwards) and the newer CEDS version of April 2021 is negligible (Supplementary Fig. 3). Thus, differences in anthropogenic aerosol emissions between the models are unlikely to impact the conclusions for the model ensemble, despite the different representation of the Chinese aerosol emission decline in the two inventories.

The model mean trend in EEI of 0.38 W m^{-2} decade^{-1} over the 2001–2019 period is, despite underestimation in all models, within the uncertainty range of the CERES trend (Fig. 1a). In the simulation with anthropogenic aerosol emissions kept constant (AERO2000), the model mean trend in EEI is reduced by 0.20 W m^{-2} decade^{-1} (intermodel range of 0.15-0.28 W m^{-2} decade^{-1}) to a much weaker trend of 0.18 W m^{-2} decade^{-1}, well outside the uncertainty range of CERES (Fig. 1b). The interannual variability is less well reproduced in all models when aerosols are kept constant, with a reduction in correlation coefficient from 0.85 to 0.76 in the model mean between BASE and AERO2000. Thus, results strongly indicate that the time evolution of aerosols needs to be included in order for the models to reproduce the observed EEI trend and variability.

The radiative response ($\alpha\Delta T_s$) is simulated by keeping all anthropogenic and natural forcings constant and only letting the sea-surface

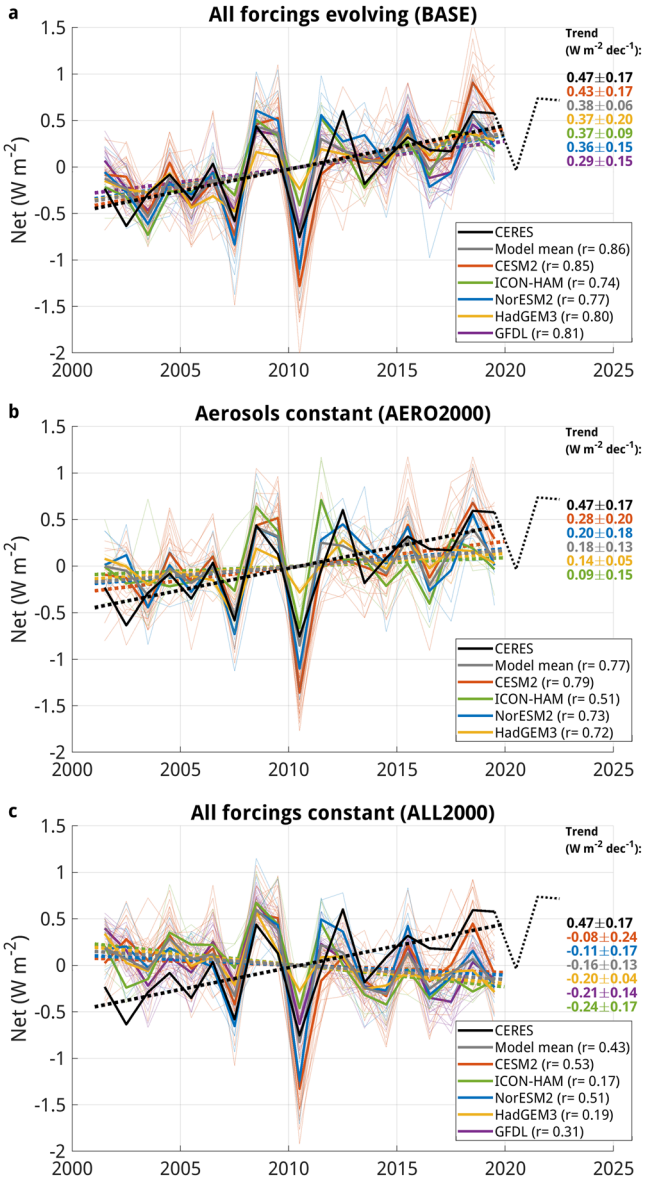

Fig. 1 | Earth's energy imbalance (EEI) trend. Comparison of the global mean annual anomaly in top-of-atmosphere net downward radiative flux between CERES and the global climate models' **a** BASE, **b** AERO2000 (anthropogenic aerosol emissions constant) and **c** ALL2000 (all anthropogenic and natural forcings constant) simulations. Individual ensemble members (thin solid coloured lines), intramodel means (thick solid colored lines), intermodel mean (thick solid grey line) and observations (thick solid black line) are shown for 2001–2019, extending to 2022 for the observations (thick dotted black line). Linear trends are shown based on intramodel means (thick dashed colored lines), intermodel means (thick dashed grey line) and observations (thick dashed black line). «Model mean» is the average of CESM2, ICON-HAM, NorESM2 and HadGEM3. Trends are based on monthly deseasonalized values and uncertainties are given as 5–95% confidence intervals based on spread between ensemble members. Correlation coefficients (r) between CERES and modelled annual anomalies are shown in the legend.

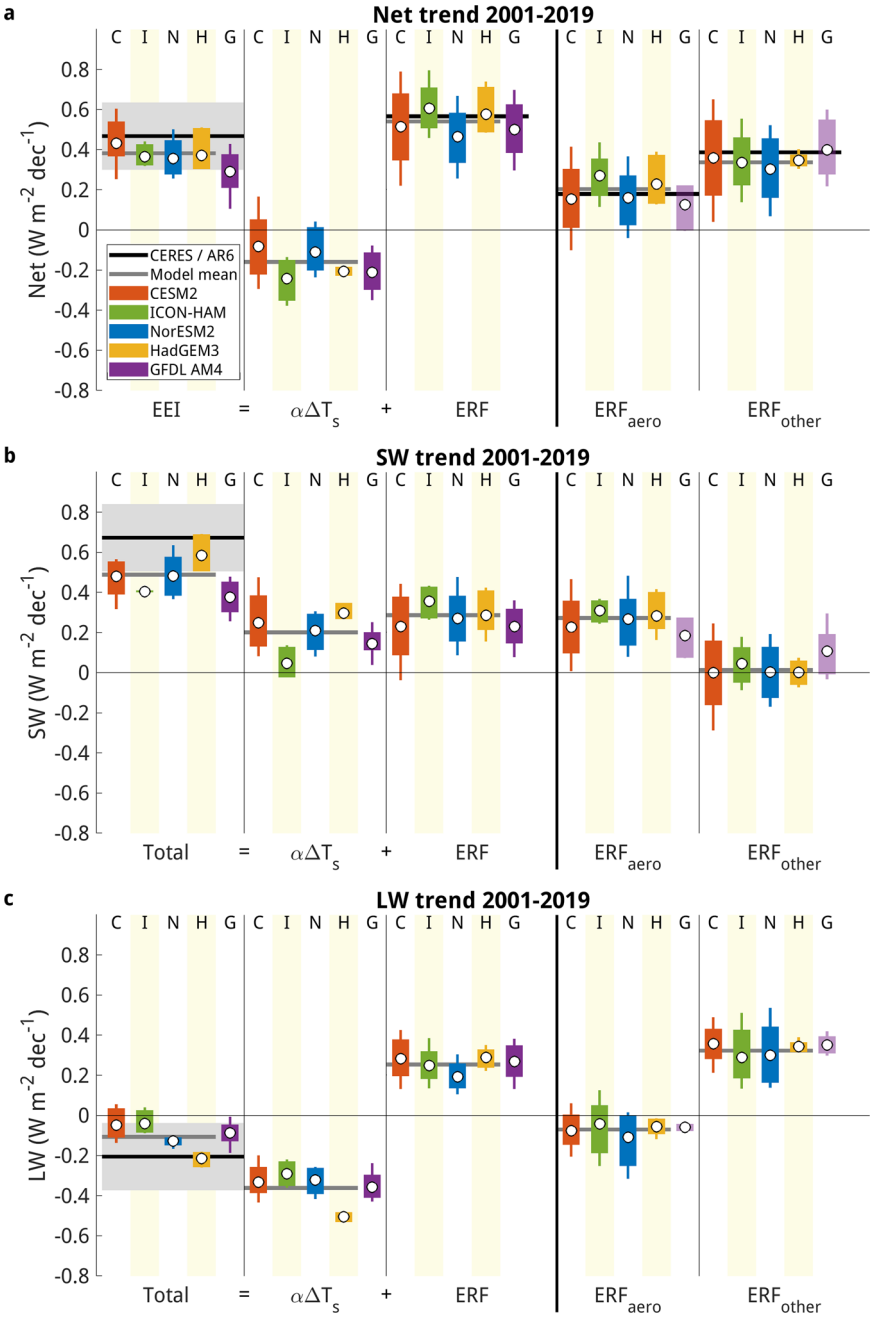

Fig. 2 | Contributing factors to Earth's energy imbalance (EEI) trend. Trend over 2001–2019 (based on deseasonalized monthly values) in top-of-atmosphere **a** net, **b** shortwave (SW) and **c** longwave (LW) downward radiative flux (i.e., EEI/total: experiment BASE) split into contributions from the radiative response ($\alpha\Delta T_s$: experiment ALL2000), and effective radiative forcing (ERF: experiments BASE-ALL2000). The ERF trend is further split into contributions from changes in aerosols (ERF_{aero}: experiments BASE-AERO2000) and other (well-mixed greenhouse gases, ozone, land use, solar) forcings (ERF_{other}: experiments AERO2000-ALL2000). Whiskers represent the 90% confidence intervals, boxes the 66% confidence intervals, and white dots show the mean for each model, based on the trends of individual ensemble members. Black lines are from CERES for EEI (including grey shading showing a 5–95% confidence interval) and IPCC AR6 for ERFs. GFDL results for ERF_{aero} and ERF_{other} (light purple boxes) are based on experiments with a different setup (RFMIP; see Methods and Supplementary Fig. 7) but are included for comparison.

temperature and sea-ice change following the prescribed input, and this simulation (ALL2000) shows a negative trend in all models with a model mean trend of –0.16 W m^{-2} decade^{-1} (intermodel range from -0.08 to -0.25 W m^{-2} decade^{-1}) (Fig. 1c). Thus, the effect of holding all forcings constant has a much larger impact on the EEI trend than holding just anthropogenic aerosol emissions constant, but the latter still has a considerable impact. In fact, the four models participating with AERO2000 simulate that the ERF due to changes in anthropogenic aerosol emissions over the recent two decades, in which several regions have reduced aerosol emissions due to air quality legislation, have led to an approximate doubling of the EEI trend (Fig. 1a, b).

Contributions to EEI trend

Differences between CERES and GCMs become larger when decomposing the radiative flux anomalies into shortwave (SW) and longwave (LW) fluxes (Fig. 2; all fluxes positive downwards). Both the observed 2001–2019 strong positive SW trend of 0.67 ± 0.17 W m^{-2} decade^{-1} and the weak negative LW trend of –0.20 ± 0.17 W m^{-2} decade^{-1} are too small in magnitude in the models, but with intermodel differences. HadGEM3 is a notable exception, showing SW and LW trends well within the uncertainty range of CERES. The weaker SW trend in GFDL compared to the other models is the main reason for this model having the weakest net EEI trend (see also Discussion section of Raghuraman et al.[7]). An evaluation of the seasonal cycle of net, SW and LW fluxes at TOA shows that the models are in good agreement with the CERES observations (Supplementary Fig. 4). Also, the four models that were part of CMIP6 (CESM2, NorESM2, HadGEM3 and GFDL) have smaller root-mean-square errors than the average of CMIP6 models when compared to observed radiative fluxes and clouds (with the exception of NorESM2 for outgoing SW radiation), and are generally among the best-performing models (Boucher et al.[21], their Figs. 18–19).

Most of the intermodel difference in the net trend in radiative response ($\alpha\Delta T_s$) results from the positive SW trend (Fig. 2), which is positive

presumably due to cloud and ice-albedo feedback. Further splitting of the radiative response trend into clear-sky and cloud radiative effect (CRE) reveals strong model diversity in CRE, indicating that the large model spread in the SW trend in radiative response is due to differences in cloud feedback (Supplementary Fig. 5a, b). The negative trend in the LW component of the radiative response, which is caused by the Planck feedback following increasing global mean surface temperature, is more similar between the models (Fig. 2c).

By taking the difference between simulations, contributions from natural and anthropogenic forcings to the EEI trend can be estimated (simulations BASE-ALL2000). The ERF trend of 0.57 W m^{-2} $decade^{-1}$ derived from the IPCC AR6 timeseries[3] (Supplementary Fig. 6) is very similar to the modelled trend (Fig. 2a). The contribution to the net ERF trend is almost equally split between SW and LW (Fig. 2b, c). However, the SW contribution to the ERF trend is entirely due to the trend in ERF of aerosols (ERF_{aero}; simulations BASE-AERO2000), in contrast to an analysis based on the Radiative Forcing Modelling Intercomparison Project (RFMIP) yielding approximately 1/3 of the SW ERF trend from greenhouse gas cloud adjustments[7]. In the shortwave, the contribution from ERF_{aero} is approximately equal to, or even larger than, the total radiative response ($\alpha\Delta T_s$). In contrast, the LW contribution is almost entirely due to other anthropogenic and natural forcings (ERF_{other}; simulations AERO2000-ALL2000). Splitting of trends into clear-sky and CRE shows that the trend in LW is predominantly related to clear-sky for ERF_{other}, strongly indicating a strengthened greenhouse effect due to increased concentrations of well-mixed greenhouse gases (Supplementary Fig. 5c, d). In total, the models show that the net trend in ERF_{aero} is a considerable part (38%; intermodel range of 30-46%) of the total ERF. RFMIP simulations indicate that the trend in ERF_{aero} from the GFDL model would have been near the lower end of this range (Fig. 2a; Supplementary Fig. 7).

The multi-model mean trend in ERF_{aero} of 0.21 W m^{-2} $decade^{-1}$ (intermodel range of 0.15-0.28 W m^{-2} $decade^{-1}$) for 2001–2019 (Fig. 2a) is higher than the GFDL AM4 trend of 0.12 W m^{-2} $decade^{-1}$ estimated for 2001-2020 using RFMIP simulations in Raghuraman et al.[7]. The trend estimate for the same GFDL simulations but for 2001–2019 still shows a relatively small trend (0.13 W m^{-2} $decade^{-1}$) (Fig. 2a; Supplementary Fig. 7). The setup of the RFMIP GFDL AM4 simulations is different from simulations in this study, most notably because pre-industrial background climatology is being used in RFMIP (e.g., for SST and sea-ice fields), but the difference in total forcing trend arising from the different setup has been deemed negligible (Table 1 in Raghuraman et al.[7]). The difference in setup is therefore unlikely to be a main cause of the weaker ERF_{aero} trend. A more likely factor is related to how different models respond to a change in aerosols, both through radiative fluxes directly and through modification of cloud properties. This uncertainty is large, and a comparison of the 2014 (relative to pre-industrial) ERF of aerosols (sum of aerosol-radiation interactions and aerosol-cloud interactions) was made between several CMIP6 models in Zelinka et al.[22] (their Table 2). Based on this, the GFDL model is among the models with the smallest negative aerosol ERF (i.e., less sensitivity to aerosols), 1.5 standard deviations away from the multi-model mean, and this may partly explain the smaller contribution of aerosols to the recent EEI trend obtained in Raghuraman et al.[7].

The four models used here (CESM2, ICON-HAM, NorESM2 and HadGEM3) have a more negative aerosol ERF than the CMIP6 multi-model mean but are collectively well within one standard deviation from the mean[22] (their Table 2; note that ICON-HAM shares the same aerosol module as the CMIP6 model MPI-ESM-1-2-HAM). Although HadGEM3 has an aerosol ERF close to the CMIP6 mean[22], this model shows a stronger trend in ERF_{aero} compared to CESM2 and NorESM2 (Fig. 2a), which both have more negative aerosol ERF. Thus, the selection of models is not expected to have a major impact on our main conclusion of a strengthening of the EEI trend due to aerosol reductions.

Global and regional trends in radiative fluxes

Figure 3 shows the 2001–2019 trend in EEI for clear-sky (SW_{clear} and LW_{clear}) and cloud radiative effect (SW_{cloud} and LW_{cloud}) (all fluxes are positive downwards). While an attribution of the all-sky trends (shown in Figs. 1–2) to individual processes requires more rigorous analysis (e.g., radiative kernel approach), there are indications of model underestimation of the global mean trend in SW_{clear}, while the modelled trend in global mean SW_{cloud} agrees very well with CERES (Fig. 3a).

Regional trend analysis shows that the weak trend in SW_{clear} is largely due to all models having the incorrect sign of the trend south of 30°S (Fig. 3d), and more specifically outside the Antarctica (Fig. 4c; Supplementary Fig. 8), presumably related to surface albedo changes. Thus, the global SW_{clear} trend is too weak in the models due to a missing component in the Southern Ocean, possibly a decrease in sea-ice, an issue that was also raised earlier[7] and which should be revisited by initiatives such as CERESMIP[11].

The positive LW_{clear} trend in CERES results from a combination of increased greenhouse effect acting to increase the trend and increasing global mean temperature acting to reduce the trend. This trend is non-existing in the model mean (Fig. 3a), due to both too negative trend north of 30°N and too weak positive trend in the tropics (Fig. 3b, c and Fig. 4d). The negative trend in LW_{cloud} is also not well reproduced by the models, and this applies to all latitude regions (Fig. 3). Part of the negative trend in LW_{cloud} from CERES has recently been attributed to cloud feedback, i.e., how the clouds are responding to warming, and the overestimation of cloud feedback in climate models is a likely main cause of the models' underestimation of the negative LW_{cloud} trend[23].

Overall, the 10-40% underestimation in the EEI trend in the models compared to CERES can be attributed to a lack of SW trend south of 30°S and an underestimated SW trend in the tropics (Fig. 3). This is partly compensated by a too strong SW trend north of 30°N and lack of negative LW trend south of 30°N. While part of the underestimation in the SW trend may be attributed to a missing component in the Southern Ocean, as explained above, it should be noted that land ice has been kept fixed in the models and that the lack of melting of land ice in the models may also contribute slightly to the underestimated trend.

Regional trends in AOD and cloud properties

Due to the role of aerosol changes in the EEI trend, it is useful to analyse the regional distribution of the trend in AOD. The GCMs are able to reproduce the AOD trend over regions dominated by anthropogenic aerosol emissions, notably AOD increases over India and reductions in the eastern US, Europe and China (Fig. 4e). ICON-HAM and HadGEM3 show stronger AOD trends than the other models (Supplementary Fig. 8), in alignment with their stronger contribution of ERF_{aero} to the trend in EEI (Fig. 2a). Positive trends in SW_{clear} are consistent north of 30°N, where aerosol emissions and AOD are reduced (Fig. 3b and Fig. 4c, e).

The positive AOD trend in MODIS over Canada and Siberia, and the negative trend over the Amazon, are not reproduced by the models (Fig. 4e). This could be related to biomass burning emissions, which are based on climatology from 2015 onwards in the models (see Methods) and recently called into question[24]. The positive AOD trend over the ocean in the southern hemisphere in MODIS is also not reproduced by the models, but various satellite products are inconsistent for this region[13].

Over regions with the strongest modelled AOD trends (eastern US, India and eastern China), the model mean trend in total cloud fraction has the same sign as the trend in AOD, but the relationship is weak and the MODIS data often shows opposite trends between AOD and cloud fraction (Fig. 4e, f). It is reassuring, however, that the modelled trends in cloud fraction over the ocean are crudely in agreement with MODIS. Trends in cloud liquid water path, which is a measure of the cloud thickness, are less similar between MODIS and the models (Fig. 4g).

We find good agreement between GCMs and CERES in terms of changes in outgoing SW fluxes and net downward fluxes over the stratocumulus-dominated eastern Pacific region (Fig. 4a; Supplementary Fig. 8), similar to Loeb, et al.[10]. Part of the large reduction in outgoing SW flux off the west coast of North America has been linked to reductions in low cloud cover following surface warming after 2014[10,23], and the models in our

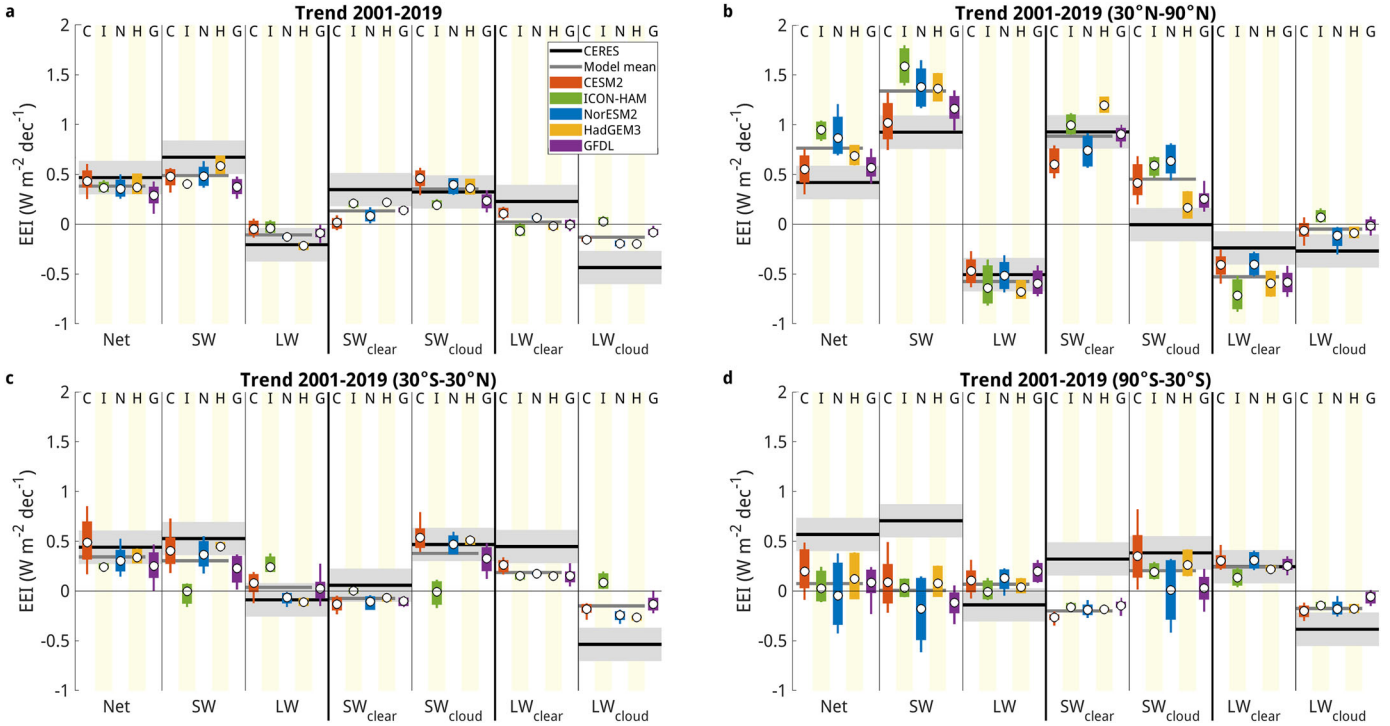

Fig. 3 | Decomposition of Earth's energy imbalance (EEI) trend. Comparison of the deseasonalized monthly 2001–2019 trend in top-of-atmosphere net, shortwave (SW) and longwave (LW) downward radiative flux between CERES and global climate models averaged over **a** the globe, **b** 30–90°N, **c** 30°S–30°N and **d** 90–30°S. SW and LW trends are shown separately for all-sky, clear-sky and the cloud radiative effect. Boxes represent the 90% and 66% confidence intervals and white dots show the mean for each model, based on the trends of individual ensemble members. Grey shading shows the 5–95% confidence interval for CERES.

study do indeed show reduced total cloud fraction in this region, consistent with MODIS.

A main finding from our model results is that the forcing due to aerosol emission reductions has led to an approximate doubling of the trend in EEI over the 2001–2019 period (Fig. 1a, b). We find that the large positive trend in all-sky net downward SW flux, which drives the positive EEI trend, is due to approximately equal contributions from ERF_{aero} and total radiative feedback. Our result showing a negligible impact on EEI of using an emission inventory that better accounts for the decline in Chinese aerosol emissions, illustrates that further research is needed to fully understand the impact of aerosols on EEI. While aerosol emission reductions are needed to improve air quality, they have added considerably to the amount of global warming we can expect without any further changes in forcing. This is likely partly responsible for the unprecedented rate of human-induced warming in the last decade[2]. Most future scenarios show rapid reductions of emissions of aerosols and their precursors[25], and it is therefore likely that such emission reductions will continue to strengthen the Earth's energy imbalance, on top of the greenhouse gas contribution. Consequently, we may expect an accelerated surface temperature warming in this decade.

Methods

CERES satellite observations

TOA radiative flux observations are from the CERES Energy Balance and Filled (EBAF) Edition 4.2[18] and consist of monthly mean SW, LW and net fluxes at a 1° × 1° spatial grid. This edition combines data from the Terra (03/2000-06/2002), Terra and Aqua (07/2002-03/2022), and the NOAA-20 (04/2022 onwards) satellites, and we use data from January 2001 to December 2022. While satellite observations cannot quantify absolute values of EEI, which is a small residual of only about 0.15% of the total incoming and outgoing radiation at TOA[18], the trend in EEI can be estimated because of the stability of the CERES instruments[26,27]. In this study, we assume a 0.20 W m^{-2} $decade^{-1}$ uncertainty in the observed SW, LW and net radiative flux trends as in Raghuraman et al.[7], but converted from a 95% confidence range to a value of 0.168 W m^{-2} $decade^{-1}$ representing the 90 (5–95)% confidence range by assuming normal distribution. The trend uncertainty is estimated based on the two contributing factors: variability in the data and radiometric stability of the instruments used to produce the data record. Loeb et al.[28] compared the longest two CERES records, from the two platforms Terra and Aqua, and found trend differences <0.1 W m^{-2} $decade^{-1}$. Also, the trend in CERES EEI is consistent with the in situ value of <0.1 W m^{-2} $decade^{-1}$ ref. 6. Therefore, for an approximately 20-year record, a total trend uncertainty (variability and stability) of 0.2 W m^{-2} $decade^{-1}$ (95% confidence range) is reasonable. Analysis of clear-sky radiative fluxes utilises the radiative fluxes of clear-sky for the total region rather than for cloud-free areas of the region (e.g., variable "toa_sw_clr_t_mon" rather than "toa_sw_clr_c_mon"), for consistency with how clear-sky radiative fluxes are calculated in the models.

MODIS satellite observations

Aerosol and cloud properties observations are from MODIS[19,20] and consist of the level-3 monthly mean dataset (D08_M3 Collection 6.1) at a 1° × 1° spatial grid from the Terra platform (starting 2002) averaged with the equivalent dataset from the Aqua platform. AOD at 550 nm is derived from the Dark Target and Deep Blue Combined Aerosol Product. It should be noted that a satellite-derived liquid water path is an in-cloud property and differs with the climate models' definition, which is averaged over the grid box.

Ocean heat uptake observations

Annual in situ estimates of the observed ocean heat uptake over 0-2,000 m for 2005-2019 from the Pacific Marine Environmental Laboratory[6] have been used for comparison to the satellite observations and model data.

Global climate models and simulations

Simulations using four state-of-the-art global climate models and multiple ensemble members have been carried out for this study, and simulations with GFDL AM4 from Raghuraman, et al.[7] have been included for comparison (Table 1). The individual ensemble members for each model use

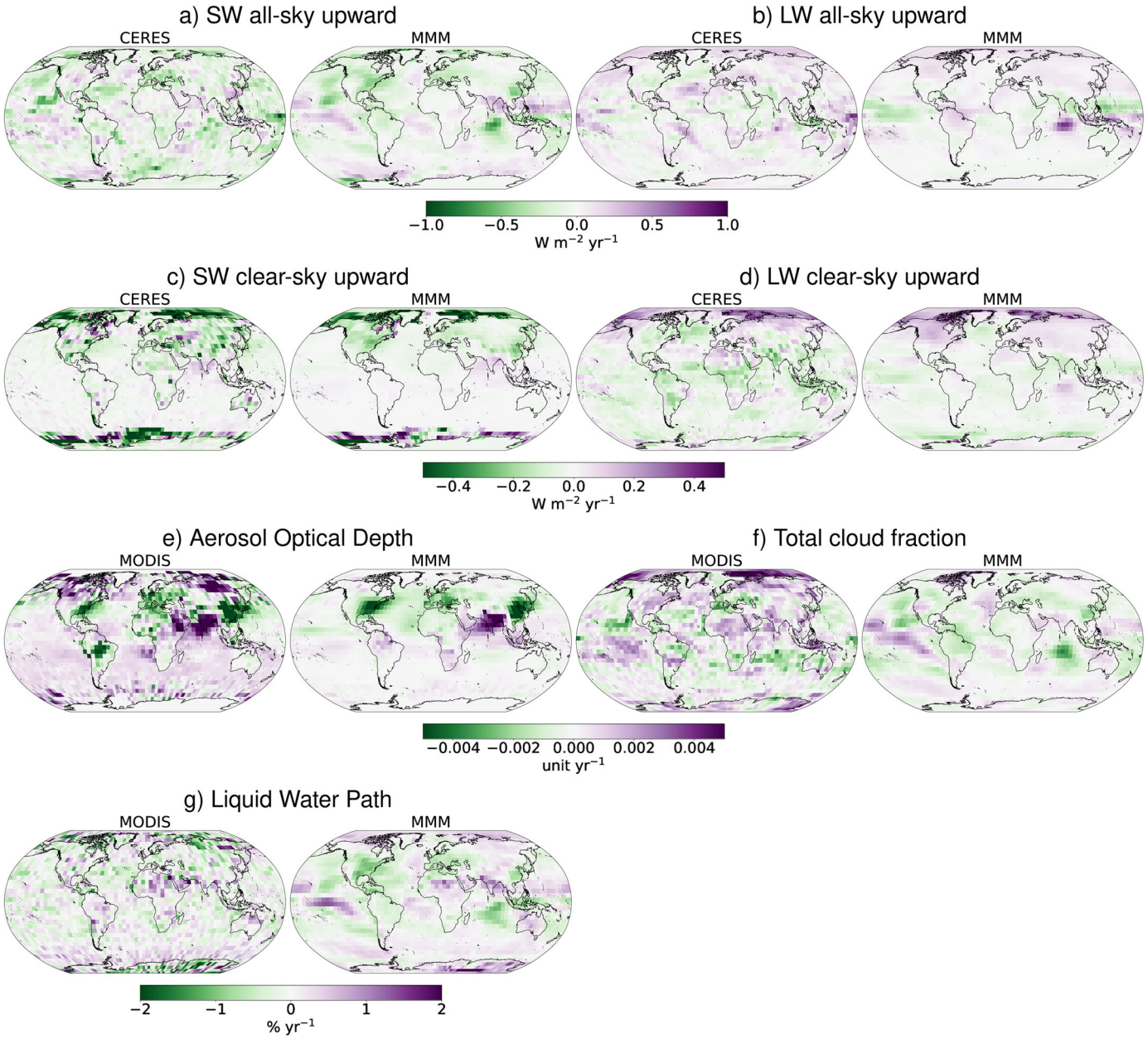

Fig. 4 | Regional trends in radiative fluxes and cloud properties. Comparison of the 2001−2019 trends between the multi-model mean (MMM) and CERES **a** SW all-sky, **b** LW all-sky, **c** SW clear-sky and **d** LW clear-sky, and MODIS **e** aerosol optical depth, **f** total cloud fraction and **g** liquid water path. Individual model results and net radiation fluxes are shown in Supplementary Fig. 8. Note that trends in radiative fluxes (**a**–**d**) show upward radiation, and therefore have positive values when more radiation is sent back to space.

identical input data except that their initial fields differ, i.e., by being initialised from a (slightly) different atmospheric state. All four models and simulations use prescribed monthly sea-surface temperature and sea-ice concentration fields for 2000–2019[29]. It has been shown that the input data used here (also known as AMIP II SST) gave a better correlation between modelled (CAM5.3) and observed (CERES) TOA radiative fluxes than when the model was forced with an alternative (HadISST) SST dataset[30], but there is likely still a structural uncertainty related to the choice of dataset used to force the models[31].

Table 1 | Models, atmospheric resolution and number of ensemble members

Model	Resolution (lon x lat x lev)	Members
CESM2-CAM6[40]	144 ×96 x 32	20
ICON-HAM[41]	R2B4 triangular grid (mesh size ~160 km) x 47	4
HadGEM3-GC3.1-LL[42]	192 × 144 × 85	3
NorESM2[43]	144 × 96 × 32	6
GFDL AM4[7,44]	144 × 90 × 33	20

Three model simulations have been carried out for each of the four models: BASE, AERO2000 and ALL2000. In BASE, anthropogenic aerosol (precursor) emissions are from the Community Emissions Data System (CEDS) version of April 2021, which goes until 2019 and builds upon the CEDS system described in McDuffie, et al.[32]. Notably, global emissions of black carbon, organic carbon and sulfur dioxide (SO_2) in recent years are lower in this newer emission inventory than in the CEDS version used in CMIP6[33]. Biomass burning emissions, well-mixed greenhouse gases and ozone concentrations, and solar insolation follow the CMIP6 historical

setup until 2014 and assume SSP2-4.5 thereafter. HadGEM3 uses the CMIP6 version of CEDS (and SSP2-4.5 from 2015) also for anthropogenic aerosol emissions.

The AERO2000 simulation is set up in the same way as BASE, except that anthropogenic aerosol emissions were representative of the year 2000 (2014 in HadGEM3) throughout the simulation. It should be noted that the radiative response caused by the aerosol forcing is not kept constant in the AERO2000 simulation as the SST and sea-ice fields are the same as in BASE. In NorESM2, biomass burning aerosol emissions were also kept constant in AERO2000, but sensitivity simulations with CESM2 indicate that the contribution from biomass burning aerosol emission changes to the EEI trend is negligible (Supplementary Fig. 9).

In the ALL2000 experiment, all anthropogenic and natural forcings are representative of the year 2000 (1850 in HadGEM3) throughout the simulation, and only the prescribed SST and sea-ice fields are transient. Additional NorESM2 sensitivity simulations with only anthropogenic forcings constant (ANTHRO2000) show that the trend in natural forcing (mainly solar and volcanic) is small and with the opposite sign compared to the trend in anthropogenic forcing (Supplementary Fig. 10).

Simulations from the GFDL model are described in Raghuraman, et al.[7] and we have analysed their "AM4 PSST ERF" (equivalent to BASE) simulation, where forcing agents are based on CMIP6 historical emissions until 2014 and SSP2-4.5 thereafter, and "AM4 PSST" (equivalent to ALL2000) simulation, where forcing agents are fixed at 2014 levels. An experiment with fixed anthropogenic aerosols (equivalent to AERO2000) is not available from that study, and the multi-model means in Figs. 1–3 are, therefore, based on the average of the CESM2, ICON-HAM, NorESM2 and HadGEM3 models. However, analysis of GFDL RFMIP simulations, which use pre-industrial SST and sea-ice fields, are shown in Fig. 2 and Supplementary Fig. 7.

Trend analysis

Deseasonalized monthly mean anomalies are calculated by taking the difference between the monthly mean value and the multi-year (2001–2019) average of the same month. Linear trends are calculated by least squares[34] on deseasonalized monthly mean time-series except for the map plots which are based on annual means and use the Mann-Kendall and Theil-Sen methods to calculate the trends[35–37]. Unless otherwise mentioned, all figures show increased downward radiation as positive trends, and vice versa. Trends in cloud radiative effects are calculated as all-sky fluxes minus clear-sky fluxes for the total region (not only cloud-free areas of the region) for both CERES and the models. The bars showing differences between experiments (e.g., the ERF bars in Fig. 2) include all possible combinations of ensemble members for each model.

Additional 60-year simulations with CESM2 using prescribed year 2000 climatology SST and sea-ice fields cycled for every year, and anthropogenic aerosol emissions representative of both 2001 and 2019, have been carried out to evaluate the method of deriving ERF_{aero} from transient BASE-AERO2000 simulations. These simulations show that ERF_{aero}, based on the 2019-2001 difference, is fairly similar between the transient simulations and the constant (year 2000 SSTs) simulations (Supplementary Fig. 11).

Data availability

CERES EBAF-TOA Edition4.2 and CERES EBAF Edition4.2 data were obtained from the NASA Langley Research Centre CERES ordering tool at https://ceres.larc.nasa.gov/data/ (downloaded 21 January 2024), and are available at https://doi.org/10.5067/TERRA-AQUA-NOAA20/CERES/EBAF-TOA_L3B004.2 and https://doi.org/10.5067/TERRA-AQUA-NOAA20/CERES/EBAF_L3B004.2, respectively. The MODIS AOD and cloud product Collection 6.1 were obtained from the NASA Goddard Earth Science Data and Information Services Centre (GES DISC) Distributed Active Archive Centre (DISC) web application available at https://giovanni.gsfc.nasa.gov/giovanni/. The ocean heat content anomaly data were obtained from the NOAA Pacific Marine Environmental Laboratory website at https://oceans.pmel.noaa.gov/upper-ocean-heat-content-data (downloaded 16 February 2024). The GCM data from CESM2, ICON-HAM, NorESM2 and HadGEM3, produced for this publication, have been made available[38] in the form of NetCDF files with https://doi.org/10.11582/2024.00024 in the NIRD research data archive: https://archive.sigma2.no/pages/public/datasetDetail.jsf?id=10.11582/2024.00024. GFDL model data from Raghuraman, et al.[7,39] are available at https://doi.org/10.5281/zenodo.4784726.

Received: 23 January 2024; Accepted: 15 March 2024;
Published online: 03 April 2024

References

1. von Schuckmann, K. et al. Heat stored in the Earth system: where does the energy go? *Earth Syst. Sci. Data* **12**, 2013–2041 (2020).
2. Forster, P. M. et al. Indicators of Global Climate Change 2022: annual update of large-scale indicators of the state of the climate system and human influence. *Earth Syst. Sci. Data* **15**, 2295–2327 (2023).
3. Forster, P. M. et al. in *Climate Change 2021: The Physical Science Basis. Contribution of Working Group I to the Sixth Assessment Report of the Intergovernmental Panel on Climate Change* (eds. V. Masson-Delmotte et al.) Ch. 7 (Cambridge University Press, 2021).
4. Loeb, N. G. et al. Toward optimal closure of the Earth's top-of-atmosphere radiation budget. *J. Clim.* **22**, 748–766 (2009).
5. Johnson, G. C., Lyman, J. M. & Loeb, N. G. Improving estimates of Earth's energy imbalance. *Nat. Clim. Chang.* **6**, 639–640 (2016).
6. Loeb, N. G. et al. Satellite and ocean data reveal marked increase in Earth's heating rate. *Geophys. Res. Lett*. **48**, https://doi.org/10.1029/2021gl093047 (2021).
7. Raghuraman, S. P., Paynter, D. & Ramaswamy, V. Anthropogenic forcing and response yield observed positive trend in Earth's energy imbalance. *Nat. Commun.* **12**, 4577 (2021).
8. Hansen, J. et al. Earth's energy imbalance: confirmation and implications. *Science* **308**, 1431–1435 (2005).
9. Ceppi, P. & Fueglistaler, S. The El Nino-Southern oscillation pattern effect. *Geophys. Res. Lett*. **48**, https://doi.org/10.1029/2021gl095261 (2021).
10. Loeb, N. G. et al. New generation of climate models track recent unprecedented changes in Earth's radiation budget observed by CERES. *Geophys. Res. Lett*. **47**, https://doi.org/10.1029/2019gl086705 (2020).
11. Schmidt, G. A. et al. CERESMIP: a climate modeling protocol to investigate recent trends in the Earth's Energy Imbalance. *Front. Clim.* **5**, https://doi.org/10.3389/fclim.2023.1202161 (2023).
12. Paulot, F., Paynter, D., Ginoux, P., Naik, V. & Horowitz, L. W. Changes in the aerosol direct radiative forcing from 2001 to 2015: observational constraints and regional mechanisms. *Atmos. Chem. Phys.* **18**, 13265–13281 (2018).
13. Quaas, J. et al. Robust evidence for reversal of the trend in aerosol effective climate forcing. *Atmos. Chem. Phys.* **22**, 12221–12239 (2022).
14. Kramer, R. J. *et al*. Observational evidence of increasing global radiative forcing. *Geophys. Res. Lett*. **48**, https://doi.org/10.1029/2020gl091585 (2021).
15. Jenkins, S. et al. Is anthropogenic global warming accelerating? *J. Clim.* **35**, 4273–4290 (2022).
16. Gryspeerdt, E., Quaas, J. & Bellouin, N. Constraining the aerosol influence on cloud fraction. *J. Geophys. Res. Atmos.* **121**, 3566–3583 (2016).
17. Cherian, R. & Quaas, J. Trends in AOD, clouds, and cloud radiative effects in satellite data and CMIP5 and CMIP6 model simulations over aerosol source regions. *Geophys. Res. Lett.* **47**, e2020GL087132 (2020).
18. Loeb, N. G. et al. Clouds and the Earth's Radiant Energy System (CERES) energy balanced and filled (EBAF) top-of-atmosphere (TOA) edition-4.0 data product. *J. Clim.* **31**, 895–918 (2018).

19. Levy, R. C. et al. The Collection 6 MODIS aerosol products over land and ocean. *Atmos. Meas. Tech.* **6**, 2989–3034 (2013).
20. Platnick, S. et al. The MODIS cloud optical and microphysical products: collection 6 updates and examples from Terra and Aqua. *IEEE Trans. Geosci. Remote Sensing* **55**, 502–525 (2017).
21. Boucher, O. et al. Presentation and evaluation of the IPSL-CM6A-LR climate model. *J. Adv. Model. Earth Syst.* **12**, e2019MS002010 (2020).
22. Zelinka, M. D., Smith, C. J., Qin, Y. & Taylor, K. E. Comparison of methods to estimate aerosol effective radiative forcings in climate models. *Atmos. Chem. Phys.* **23**, 8879–8898 (2023).
23. Raghuraman, S. P., Paynter, D., Menzel, R. & Ramaswamy, V. Forcing, cloud feedbacks, cloud masking, and internal variability in the cloud radiative effect satellite record. *J. Clim.* **36**, 4151–4167 (2023).
24. Fasullo, J. T. et al. Spurious late historical-era warming in CESM2 driven by prescribed biomass burning emissions. *Geophys. Res. Lett.* **49**, e2021GL097420 (2022).
25. Chen, D. et al. in *Climate Change 2021: The Physical Science Basis. Contribution of Working Group I to the Sixth Assessment Report of the Intergovernmental Panel on Climate Change* (eds. V. Masson-Delmotte et al.) Ch. 1 (Cambridge University Press, 2021).
26. Shankar, M., Su, W., Manalo-Smith, N. & Loeb, N. G. Generation of a seamless Earth radiation budget climate data record: a new methodology for placing overlapping satellite instruments on the same radiometric scale. *Remote Sens.* **12**, 2787 (2020).
27. Shankar, M. et al. Evaluating the radiometric performance of the clouds and the Earth's Radiant Energy System (CERES) instruments on Terra and Aqua over 20 years. *IEEE Trans. Geosci. Remote Sensing* **61**, 1–11 (2023).
28. Loeb, N. G. et al. Evaluating twenty-year trends in Earth's energy flows from observations and reanalyses. *J. Geophys. Res. Atmos.* **127**, e2022JD036686 (2022).
29. Hurrell, J. W., Hack, J. J., Shea, D., Caron, J. M. & Rosinski, J. A new sea surface temperature and sea ice boundary dataset for the Community Atmosphere Model. *J. Clim.* **21**, 5145–5153 (2008).
30. Zhou, C., Zelinka, M. D., Dessler, A. E. & Wang, M. Greater committed warming after accounting for the pattern effect. *Nat. Clim. Chang.* **11**, 132–136 (2021).
31. Andrews, T. et al. On the effect of historical SST patterns on radiative feedback. *J. Geophys. Res. -Atmos*. **127**, https://doi.org/10.1029/2022jd036675 (2022).
32. McDuffie, E. E. et al. A global anthropogenic emission inventory of atmospheric pollutants from sector- and fuel-specific sources (1970–2017): an application of the Community Emissions Data System (CEDS). *Earth Syst. Sci. Data* **12**, 3413–3442 (2020).
33. Hoesly, R. M. et al. Historical (1750-2014) anthropogenic emissions of reactive gases and aerosols from the Community Emissions Data System (CEDS). *Geosci. Model Dev.* **11**, 369–408 (2018).
34. Greene, C. A. et al. The climate data toolbox for MATLAB. *Geochem. Geophys. Geosyst.* **20**, 3774–3781 (2019).
35. Kendall, M. G. A new measure of rank correlation. *Biometrika* **30**, 81–93 (1938).
36. Theil, H. in *Henri Theil's Contributions to Economics and Econometrics: Econometric Theory and Methodology* (eds. B. Raj & J. Koerts) 345–381 (Springer Netherlands, 1992).
37. Sen, P. K. Estimates of the regression coefficient based on Kendall's Tau. *J. Am. Stat. Assoc.* **63**, 1379–1389 (1968).
38. Hodnebrog, Ø. et al. Recent reductions in aerosol emissions have increased Earth's energy imbalance [Data set]. *Norstore*, https://doi.org/10.11582/2024.00024 (2024).
39. Raghuraman, S. P., Paynter, D. & Ramaswamy, V. Anthropogenic forcing and response yield observed positive trend in Earth's energy imbalance (Data) [Data set]. *Zenodo* https://doi.org/10.5281/zenodo.4784726 (2021).
40. Danabasoglu, G. et al. The Community Earth System Model version 2 (CESM2). *J. Adv. Model. Earth Syst.* **12**, 35 (2020).
41. Salzmann, M. et al. The Global Atmosphere-aerosol Model ICON-A-HAM2.3–initial model evaluation and effects of radiation balance tuning on aerosol optical thickness. *J. Adv. Model. Earth Syst.* **14**, e2021MS002699 (2022).
42. Williams, K. D. et al. The Met Office Global Coupled Model 3.0 and 3.1 (GC3.0 and GC3.1) configurations. *J. Adv. Model. Earth Syst.* **10**, 357–380 (2018).
43. Seland, Ø. et al. Overview of the Norwegian Earth System Model (NorESM2) and key climate response of CMIP6 DECK, historical, and scenario simulations. *Geosci. Model Dev.* **13**, 6165–6200 (2020).
44. Zhao, M. et al. The GFDL Global Atmosphere and Land Model AM4.0/LM4.0:1. simulation characteristics with prescribed SSTs. *J. Adv. Model. Earth Syst.* **10**, 691–734 (2018).

Acknowledgements

Ø.H., G.M., C.J., T.A., P.F., H.J. and J.Q. received funding from the European Union's Horizon 2020 research and innovation programme under grant agreement 820829 (CONSTRAIN). Ø.H., G.M., C.J., D.J.L.O. and M.S. received support from the Research Council of Norway (295046). T.A. was supported by the Met Office Hadley Centre Climate Programme funded by BEIS. Storage and CESM2 simulations took place on resources provided by Sigma2—the National Infrastructure for High-Performance Computing and Data Storage in Norway (NS9188K/NN9188K). Jing Feng is acknowledged for comments and suggestions on an internal review of the manuscript.

Author contributions

Ø.H. performed the CESM2 simulations, did most of the analysis, led the work and wrote the paper. G.M. had the original idea and initiated the work, gave regular input and contributed to the writing. C.J. did a regional analysis of CERES, MODIS and model data, and contributed to the writing. T.A. contributed with HadGEM3 simulations and expertise, and contributed to the writing. P.M.F. contributed with expertise and to the writing. H.J. contributed with ICON-HAM simulations and to the writing. N.G.L. contributed with CERES expertise and to the writing. D.J.L.O. contributed with NorESM2 simulations and to the writing. D.P. contributed with GFDL AM4 model expertise and to the writing. J.Q. contributed with ICON-HAM expertise and to the writing. S.P.R. contributed with GFDL AM4 model expertise and to the writing. M.S. contributed with NorESM2 expertise and to the writing.

Competing interests

The authors declare no competing interests.

Additional information

Supplementary information The online version contains supplementary material available at https://doi.org/10.1038/s43247-024-01324-8.

Correspondence and requests for materials should be addressed to Øivind Hodnebrog.

Peer review information *Communications Earth & Environment* thanks the anonymous reviewers for their contribution to the peer review of this work. Primary handling editor: Aliénor Lavergne. A peer review file is available.